JOURNAL OF GEOPHYSICAL RESEARCH, VOL. 115, C03012, doi:10.1029/2009JC005657, 2010

A census of eddy activities in the South China Sea during 1993–2007

Peng Xiu,[1] Fei Chai,[1] Lei Shi,[1] Huijie Xue,[1] and Yi Chao[2]

Received 21 July 2009; revised 5 October 2009; accepted 14 October 2009; published 10 March 2010.

[1] Numerous mesoscale eddies occur each year in the South China Sea (SCS), but their statistical characteristics are still not well documented. A Pacific basin-wide three-dimensional physical-biogeochemical model has been developed and the result in the SCS subdomain is used to quantify the eddy activities during the period of 1993–2007. The modeled results are compared with a merged and gridded satellite product of sea level anomaly by using the same eddy identification and tracking method. On average, there are about 32.9 ± 2.4 eddies predicted by the model and 32.8 ± 3.4 eddies observed by satellite each year, and about 52% of them are cyclonic eddies. The radius of these eddies ranges from about 46.5 to 223.5 km, with a mean value of 87.4 km. More than 70% of the eddies have a radius smaller than 100 km. The mean area covered by these eddies each year is around 160,170 km^2, equivalent to 9.8% of the SCS area with water depths greater than 1000 m. Linear relationships are found between eddy lifetime and eddy magnitude and between eddy vertical extent and eddy magnitude, showing that strong eddies usually last longer and penetrate deeper than weak ones. Interannual variations in eddy numbers and the total eddy-occupied area indicate that eddy activities in the SCS do not directly correspond to the El Niño–Southern Oscillation events. The wind stress curls are thought to be an important but not the only mechanism of eddy genesis in the SCS.

Citation: Xiu, P., F. Chai, L. Shi, H. Xue, and Y. Chao (2010), A census of eddy activities in the South China Sea during 1993–2007, *J. Geophys. Res.*, *115*, C03012, doi:10.1029/2009JC005657.

1. Introduction

[2] The South China Sea (SCS) is the largest semi-enclosed marginal sea in the northwest Pacific, with a total surface area of 3.5 million km^2 and an average depth of over 2000 m (Figure 1). SCS climate is part of the East Asia monsoon system [*Wyrtki*, 1961; *Liu and Xie*, 1999; *Gan et al.*, 2006]. In this paper, seasons always refer to those for the Northern Hemisphere, for example, summer refers to June, July, and August. In winter, the SCS is dominated by the strong northeasterly monsoon, whereas in summer the winds reverse direction to southwesterly. The alternating monsoons in winter and summer lead to the transformation of the upper circulation in the SCS [e.g., *Xue et al.*, 2004; *Su*, 2004].

[3] The patterns and variations of the seasonal circulation in the SCS are largely driven by the monsoon system [*Liu et al.*, 2008]. There is a basin-wide cyclonic gyre in winter, while in summer there is a cyclonic gyre north of about 12° N and an anticyclonic gyre south of it. The circulation in the northern SCS is strongly influenced by the inflows and outflows through Luzon Strait and Taiwan Strait [*Hu et al.*, 2000]. The Kuroshio enters the SCS year-round through the Luzon Strait. The Kuroshio intrusion forms an apparent anticyclonic current loop west of the Luzon Strait most of the year. The anticyclonic current loop is shown to have profound influences on the water properties on the northern shelf region [*Xue et al.*, 2004]. A substantial amount of outflow is through the Taiwan Strait in the north year-round. In summer, as the southwesterly winds prevail, a strong wind stress curl occurs offshore of the Vietnam coast, resulting in an anticyclonic eddy that advects the cold coastal water offshore to the interior SCS. In addition to the seasonal variation, the SCS circulation also shows interannual variation related to El Niño–Southern Oscillation (ENSO) events [*Kuo et al.*, 2004; *Liu et al.*, 2004; *Fang et al.*, 2006]. The Luzon Strait transport, as an index for the SCS throughflow, is revealed as a key process that conveys the impact of ENSO to the SCS [*Qu et al.*, 2004]. In the surface layer, the intrusion of Pacific waters through the Luzon Strait depends on the local wind and tends to be weaker during El Niño years and stronger during La Niña years [*Qu et al.*, 2005]. As part of the Pacific tropical gyre, the Luzon Strait transport is also influenced by variations of the North Equatorial Current (NEC), which bifurcates to become the northward-flowing Kuroshio [*Qu et al.*, 2009]. Results from high-resolution general circulation models (GCM) suggest that the bifurcation of the NEC shifts northward during El Niño years and leads to a minimum transport in the Kuroshio east of Luzon. As a result, more intrusions of Pacific waters through the

[1] School of Marine Sciences, University of Maine, Orono, Maine, USA.
[2] Jet Propulsion Laboratory, California Institute of Technology, Pasadena, California, USA.

0148-0227/10/2009JC005657$09.00

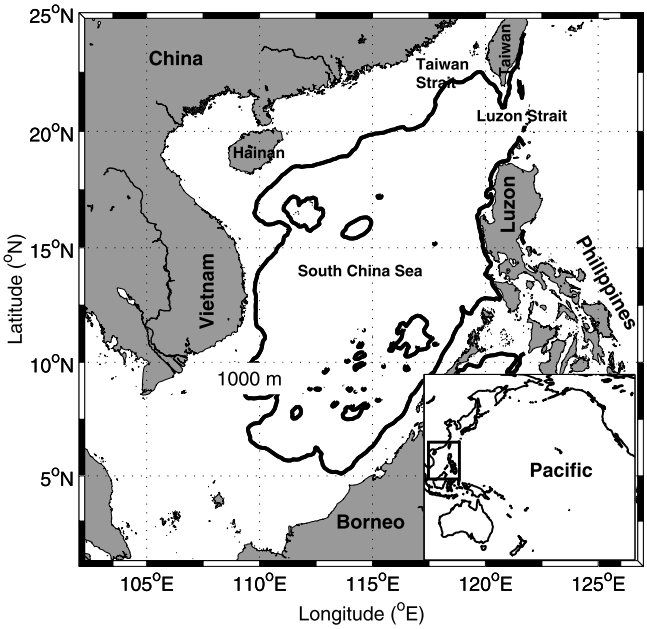

Figure 1. Map of the SCS. The contour lines are 1000 m isobaths.

Luzon Strait take place due to the weakening barrier of Kuroshio [*Yaremchuk and Qu*, 2004]. This situation tends to be reversed during La Niña years. Using the Island Rule, *Wang et al.* [2006] indicates that the interannual variability of the Luzon Strait transport is largely related to the wind stress in the western and central equatorial Pacific, which regulates the bifurcation of the NEC and the Kuroshio east of Luzon.

[4] Oceanic eddies are often more energetic than the surrounding currents. They can transport heat, mass, momentum, and biogeochemical properties from their regions of formation to remote areas. They are an important component of dynamical oceanography across the range of scales [*Wunsch*, 1999; *Qiu and Chen*, 2005; *Chaigneau et al.*, 2008]. Active eddies embedded in the SCS gyres have been examined by several studies [e.g., *Shaw et al.*, 1999; *Fang et al.*, 2002]. *Soong et al.* [1995] discovered a cold core eddy west of Luzon Island using TOPEX/Poseidon (T/P) altimetry, AVHRR temperature images, and drifter data. *Chi et al.* [1998] simulated the warm and cold core eddies in the SCS deep basin with the Princeton Ocean Model (POM). *Li et al.* [1998] found an anticyclonic eddy centered at about 117.5°E, 21°N east of Dongsha Island during their hydrographic surveys. They argued this eddy originated from the Kuroshio, while the recent study of *Yuan et al.* [2007] shows that this eddy appears to be generated from northwest of the Luzon Island instead of shed from the Kuroshio in the Luzon Strait. Based on the satellite altimetry data, *Hwang and Chen* [2000] examined the circulation and eddies in the SCS. Significant mesoscale variabilities in the SCS were found in two narrow strips north of 10°N by *Wang et al.* [2000]. *Jia and Liu* [2004] investigated the variation of Kuroshio intrusion and eddy shedding at the Luzon Strait using 1992–2001 altimeter data. Using a numerical model, *Jia et al.* [2005] studied the mechanism of the anticyclonic eddy's shedding from the Kuroshio bend in Luzon Strait. With a numerical model, *Wu and Chiang* [2007] found that the mesoscale eddies have the same propagation speed as Rossby waves, and the seasonal variability of the Kuroshio intrusion results in more eddies in winter than in summer. *D. Wang et al.* [2008] analyzed in detail the temporal and spatial evolution of two eddies in the northeastern SCS during winter using sea level anomaly (SLA) data, drifter data, geostrophic currents and sea surface temperature (SST) data. They showed that the propagation speed of eddies is similar to the phase speed of Rossby waves in the northern SCS. *G. Wang et al.* [2008] showed that, during the winter monsoon, alternating clusters of cyclonic and anticyclonic eddies are found northwest of the Luzon Strait. They suggested these clusters of anticyclonic and cyclonic eddies are correlated, respectively, to the strong negative and positive wind stress curls because of the orographic effects. Several other studies have also associated some of the eddies observed in the SCS with wind forcing [e.g., *Metzger*, 2003].

[5] Despite previous efforts to study the SCS eddy field, there is still not a thorough statistical assessment of eddy activities from numerical models. *Wang et al.* [2003] did a statistical study on mesoscale eddies using a merged SSHA data set and showed that eddies are mainly grouped into four geographic zones according to known eddy generation mechanisms. They used only 8 year time series from 1993 to 2000 due to the limitation of satellite data. The launch of a new altimeter, Jason-1 since 2002 which was designed to offer consistent sea level record with previous altimeter TOPEX/Poseidon, provides an opportunity to examine the eddy activities at a long-term basis. Thus, we expand on *Wang et al.*'s [2003] study, applying an objective eddy identification algorithm to a merged sea level anomaly (MSLA) satellite data set from 1993 to 2007. Moreover, we also conducted a three-dimensional model simulation of the 1993–2007 period to compare with the satellite data. The advantage of the numerical model is it also shows the vertical structures of cyclonic and anticyclonic eddies, which could further help us to study the role of eddies in the biogeochemical cycles in our future research. Our goal in this work is to conduct an eddy census systematically including the numbers, sizes, lifetimes and tracks in the SCS both from numerical model results and satellite data.

[6] The organization of this paper is as follows. Section 2 describes the numerical model and the satellite data, as well as the methods used to identify and track eddies. Section 3 focuses on the results and discussions including comparisons of eddy kinetic energy, eddy numbers, and eddy area, etc. between the model results and satellite observations, seasonal variabilities of eddy activities, the genesis, the propagation and the lifetime of both cyclonic and anticyclonic eddies. Section 4 summarizes the findings and discusses their implications.

2. Data and Methods

2.1. Ocean Model

[7] The physical circulation model used in this study is based on the Regional Ocean Model System (ROMS), which represents an evolution in the family of terrain-following vertical coordinate models. ROMS solves the hydrostatic, primitive equations with horizontal curvilinear coordinates. *Wang and Chao* [2004] have configured the

ROMS circulation model for the Pacific Ocean (45°S to 65° N, 99°E to 70°W) at 50 km resolution, with realistic geometry and topography. We followed the approach of *Wang and Chao* [2004] for setting up the circulation model, but increase the horizontal resolution to 12.5 km for the entire Pacific Ocean domain. There are 30 levels in the vertical. Near the two closed northern and southern walls, a sponge layer with a thickness of 5° from the walls is applied for temperature, salinity, and nutrients. The treatment of the sponge layer consists of a decay term k(T* − T) in the temperature equation (k(S* − S) for salinity equation, k(N* − N) for nutrient and carbon equations), which restores the modeled variables to the observed temperature T* (salinity S*, nutrients N*) field at the two closed walls. The value of k varies smoothly from 1/30 day^{-1} at the walls to zero at 5° away from them.

[8] Initialized with climatological temperature and salinity from the World Ocean Atlas (WOA) 2001, the Pacific ROMS model has been forced with the climatological NCEP/NCAR reanalysis of air-sea fluxes [*Kalnay et al.*, 1996] for several decades in order to reach quasi-equilibrium. The model is then integrated for the period of 1993–2007 forced with daily air-sea fluxes of heat and freshwater from the NCEP/NCAR reanalysis [*Kalnay et al.*, 1996]. The heat flux is derived from the short- and long-wave radiations, sensible and latent heat fluxes that are calculated using the bulk formula with prescribed air temperature and relative humidity. The freshwater flux is derived from the prescribed precipitation and the evaporation converted from the latent heat release. River discharges are not included in the model configuration. The blended daily sea wind with a resolution of 0.25° [*Zhang et al.*, 2006] is used to calculate the surface wind stress based on the bulk formula of *Large and Pond*'s [1982]. Three day averaged sea level anomaly and other variables are saved for the entire Pacific domain, but the model output for the SCS (domain of 2°–26°N, 103°–122°E) are used in the analysis.

2.2. Satellite Data

[9] A merged and gridded satellite product of MSLA (Maps of Sea Level Anomaly) from 1993 to 2007 produced and distributed by AVISO (http://www.aviso.oceanobs.com/) based on TOPEX/Poseidon, Jason 1, ERS-1, and ERS-2 data [*Ducet et al.*, 2000] was used to compare with our model results. This product consists of maps of 7 day intervals on a 0.25° resolution in both latitude and longitude. It has been corrected for all geophysical errors. However, due to the coarse resolution both in space and time relative to the model outputs, this product may not resolve small-scale or short-lived eddies as well as our model. Comparisons between them are only taken qualitatively.

2.3. Eddy Detection Methodology

[10] The Okubo-Weiss method was used in this study to identify eddies [*Okubo*, 1970; *Weiss*, 1991]. This method has been widely applied to SLA fields from the Mediterranean Sea [*Isern-Fontanet et al.*, 2003, 2006; *d'Ovidio et al.*, 2009], the Tasman Sea [*Waugh et al.*, 2006], the Gulf of Alaska [*Henson and Thomas*, 2008], the eastern South Pacific Ocean [*Chaigneau et al.*, 2008], the Hawaiian Islands [*Calil et al.*, 2008], and globally [*Chelton et al.*, 2007]. During each time step, the velocity field is derived from SLA maps assuming geostrophic balance

$$u = -\frac{g}{f}\frac{\partial h}{\partial y},\ v = \frac{g}{f}\frac{\partial h}{\partial x}, \tag{1}$$

where h is the SLA, g is gravitational acceleration, and f is the Coriolis parameter. The Okubo-Weiss parameter of two-dimensional disturbance field is defined by

$$W = s_n^2 + s_s^2 - \omega^2, \tag{2}$$

where s_n is the normal component of strain, s_s is the shear component, and ω is the relative vorticity of the flow, defined by, respectively

$$s_n = \frac{\partial u}{\partial x} - \frac{\partial v}{\partial y},\ s_s = \frac{\partial v}{\partial x} + \frac{\partial u}{\partial y},\ \omega = \frac{\partial v}{\partial x} - \frac{\partial u}{\partial y}. \tag{3}$$

The general structure of an eddy consists of a vorticity-dominated region (eddy core, for both cyclonic and anticyclonic eddies) surrounded by a strain-dominated circulation cell. The Okubo-Weiss parameter, W, separates the flow field into either strain dominated (W > 0) or vorticity dominated (W < 0). Therefore, we define the eddy core as a coherent region with high-vorticity threshold of $W < -0.2\sigma_w$, where σ_w is the standard deviation of W, obtained from each time step of the entire study area.

[11] The main advantage of Okubo-Weiss detecting method is that it is able to distinguish regions dominated by eddies from their surrounding regions precisely with only one derived parameter, W by merely using SLA data, which is quite simple for the implementation of long-term altimeter data. As pointed out by *Basdevant and Philipovitch* [1994], however, the Okubo-Weiss criterion is restricted to the core of the vortices and may underestimate the diameter hence the area of an eddy [*Isern-Fontanet et al.*, 2003; *Doglioli et al.*, 2007; *Henson and Thomas*, 2008]. In order to better identify eddy core area, another criterion was introduced in this analysis and the whole identification procedure can be summarized according to the following steps:

[12] 1. Use Okubo-Weiss criterion to determine a data point as an eddy point ($W < -0.2\sigma_W$) or otherwise. Adjoining eddy points are grouped as the first guess of eddies.

[13] 2. Determine the center of an eddy using the mean longitude and mean latitude for the eddy points that belong to an enclosed area.

[14] 3. Calculate the mean SLA and the distances between the eddy center and the grid points identified as the same eddy.

[15] 4. Search the SLA map around the eddy center with a radius of the longest distance calculated by step (2). For an anticyclonic (cyclonic) eddy, data points within the search area with SLA values higher (lower) than the mean SLA calculated by step (2) are then relabeled as the eddy points.

[16] 5. Any eddies with a lifetime shorter than 30 days and spatial radius smaller than 45 km are discarded (eddy lifetime is determined by a connectivity algorithm described below).

[17] 6. Because SLA data obtained nearshore are unreliable, if the center of one identified eddy exists over

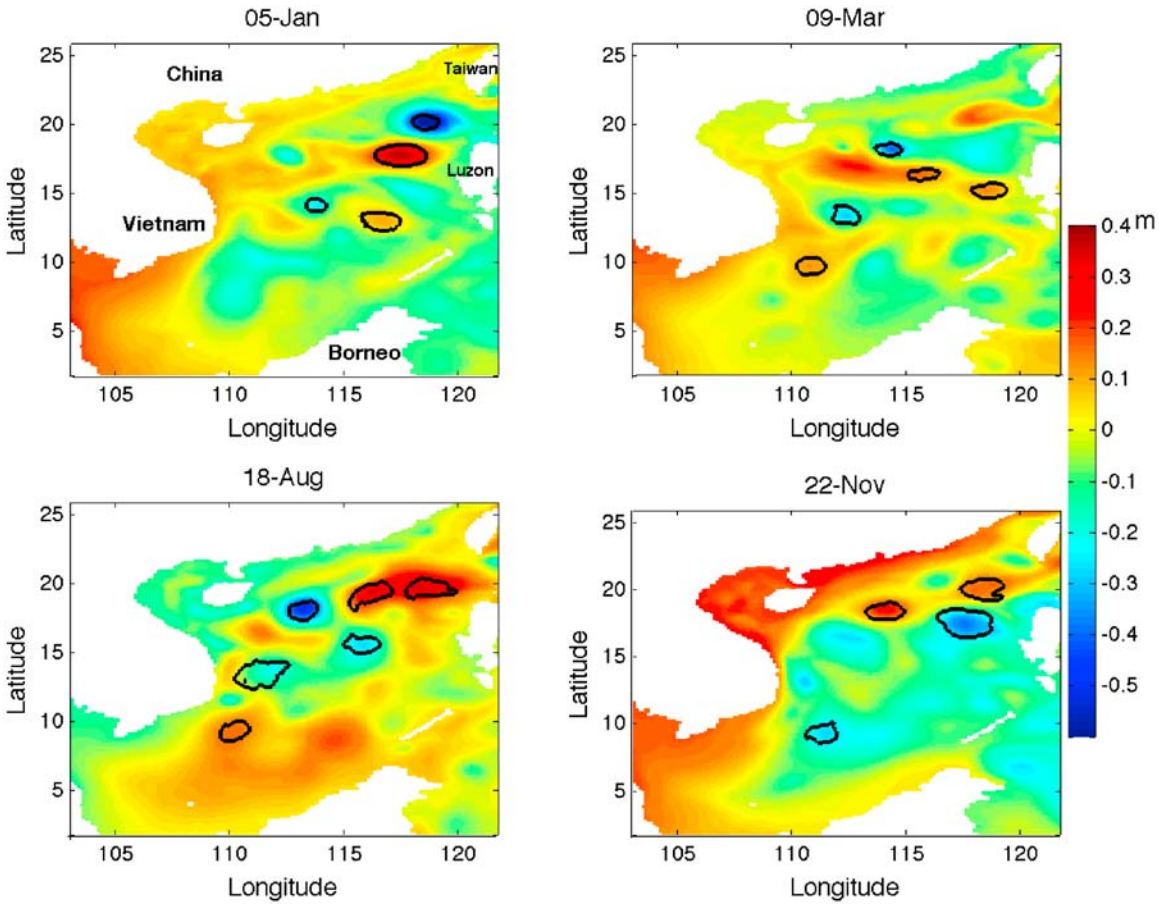

Figure 2. Four example SLA maps in year 2002. Black lines denote eddy cores identified by the Okubo-Weiss parameter.

water depths shallower than 1000 m, we discard it from the analysis.

[18] Using the above procedures, we make sure the pixel with low/high SLA value that is adjacent to the cyclonic/anticyclonic eddy but missed by the Okubo-Weiss criterion can be relabeled as cyclonic/anticyclonic eddy, thus providing a better representation of eddy core area.

[19] To examine the vertical structures of eddies, we first apply step (1) to each vertical layer of the modeled velocity field. We then search the eddy points as identified from the

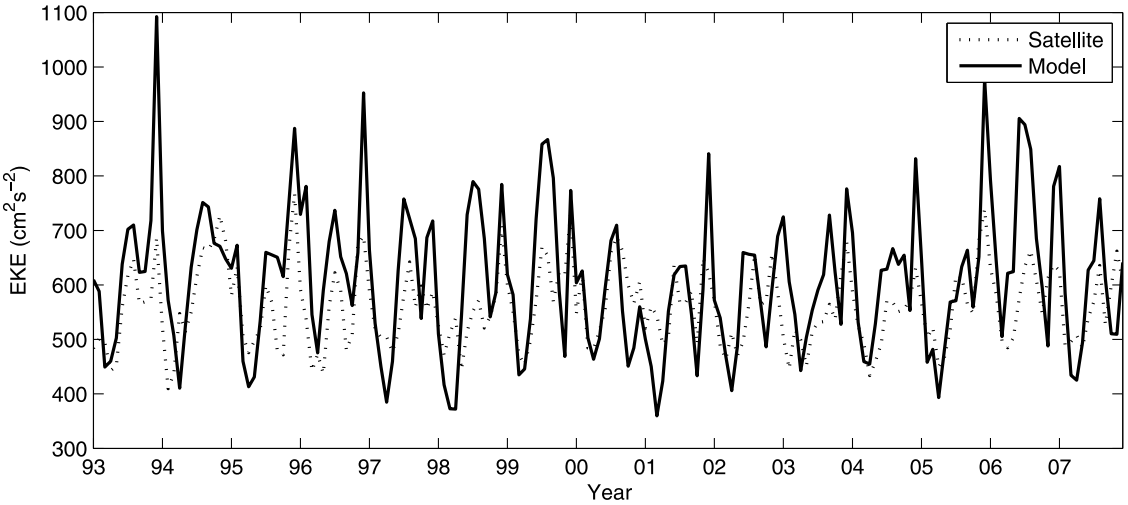

Figure 3. Comparison of EKE time series between the model and the satellite data. The time domain is 1993–2007.

Table 1. Comparison of Eddy Characteristics Between the Model and Satellite Observations

	Data	Minimum	Maximum	Mean	Standard Deviation
EKE ($cm^2\ s^{-2}$)	Model	359.7	1092.4	609.7	130.0
EKE ($cm^2\ s^{-2}$)	Satellite	409.6	767.3	559.9	72.3
Numbers	Model	28	37	32.9	2.4
Numbers	Satellite	27	38	32.8	3.4
Total Area (km^2)	Model	46,774	301,550	160,170	50,683
Total Area (km^2)	Satellite	55,773	202,490	127,880	30,902
Total Area Ratio (%)[a]	Model	1.24	7.98	4.24	1.34
Total Area Ratio (%)[a]	Satellite	1.26	4.57	2.88	0.70

[a]Total eddy area divided by the whole SCS domain shown in Figure 1.

surface SLA map at different vertical layers, and the vertical extent of an eddy is determined as the depth at which the spatial radius of the eddy becomes smaller than 45 km. Finally, eddy trajectories are determined from map to map by using a connectivity algorithm (see detailed description by *Henson and Thomas* [2008]). This algorithm groups pixels that are adjacent in longitude, latitude, and time and works well in the area where eddies are spatially separated from each other. It is much simpler and faster than other complicated tracking algorithms based on the geometrical distance from one eddy center to another [e.g., *Isern-Fontanet et al.*, 2003, 2006].

3. Results and Discussions

[20] Four example SLA maps in year 2002 are plotted in Figure 2. Overlaid contour lines are the identified eddies using the procedure described above. This method locates the eddy cores, with closed SLA highs corresponding to anticyclonic eddies and closed SLA lows corresponding to cyclonic eddies. Some local low/high SLA in Figure 2 that are not distinguished as eddies are probably because they are either too small or are short lived.

3.1. Eddy Kinetic Energy

[21] To evaluate the model performance, we first compared the eddy kinetic energy (EKE) for the whole SCS domain (2°–26°N, 103°–122°E) between the model and satellite data. EKE is produced by the perturbations of the surface velocity and is thought to be dynamically related to eddy activities. Monthly time series of spatially averaged EKE are plotted in Figure 3. The modeled EKE varies from 359.7 to 1092.4 $cm^2\ s^{-2}$ with pronounced seasonal variations. EKE in autumn is significantly higher than other seasons, which is consistent with previous studies [e.g., *He et al.*, 2002]. Besides the seasonal cycle, prominent interannual variability is also found. Model shows that high EKE

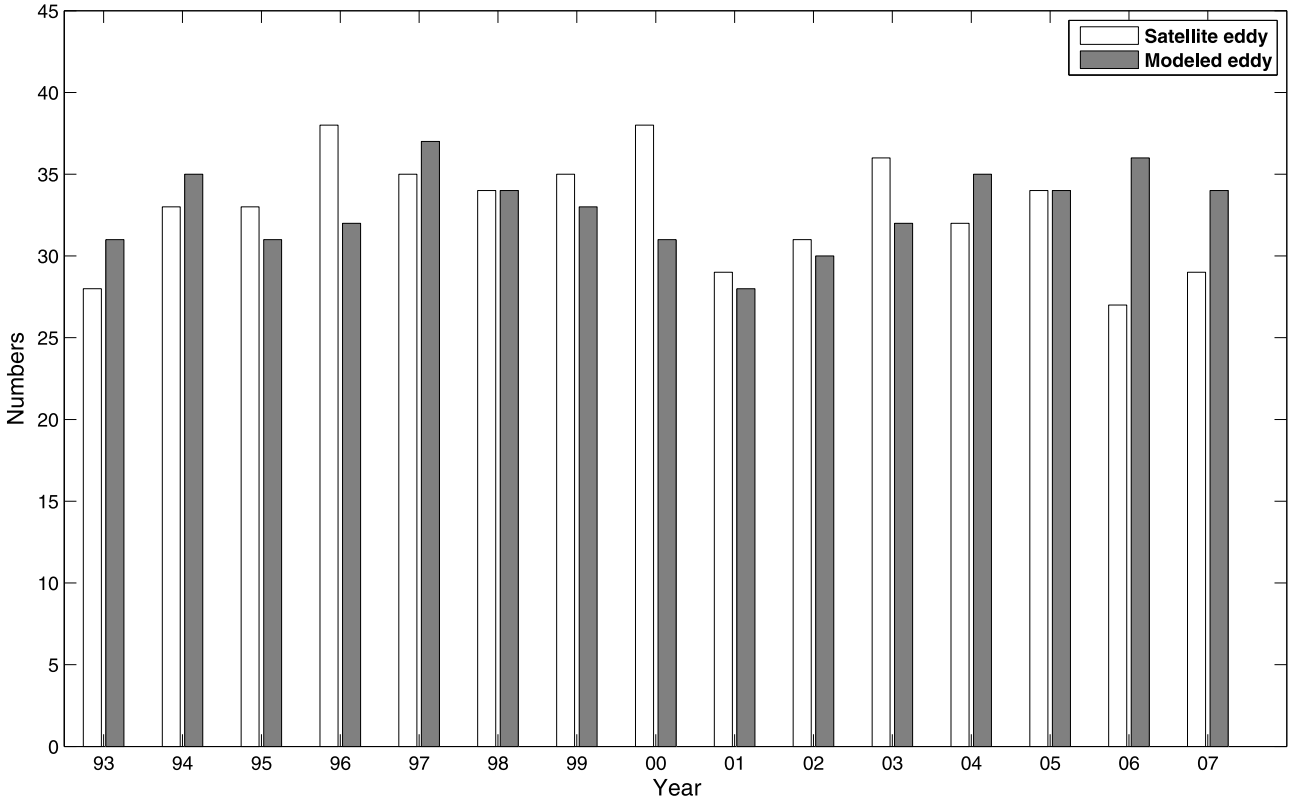

Figure 4. The number of eddies (cyclonic plus anticyclonic) identified each year both from the model and the satellite.

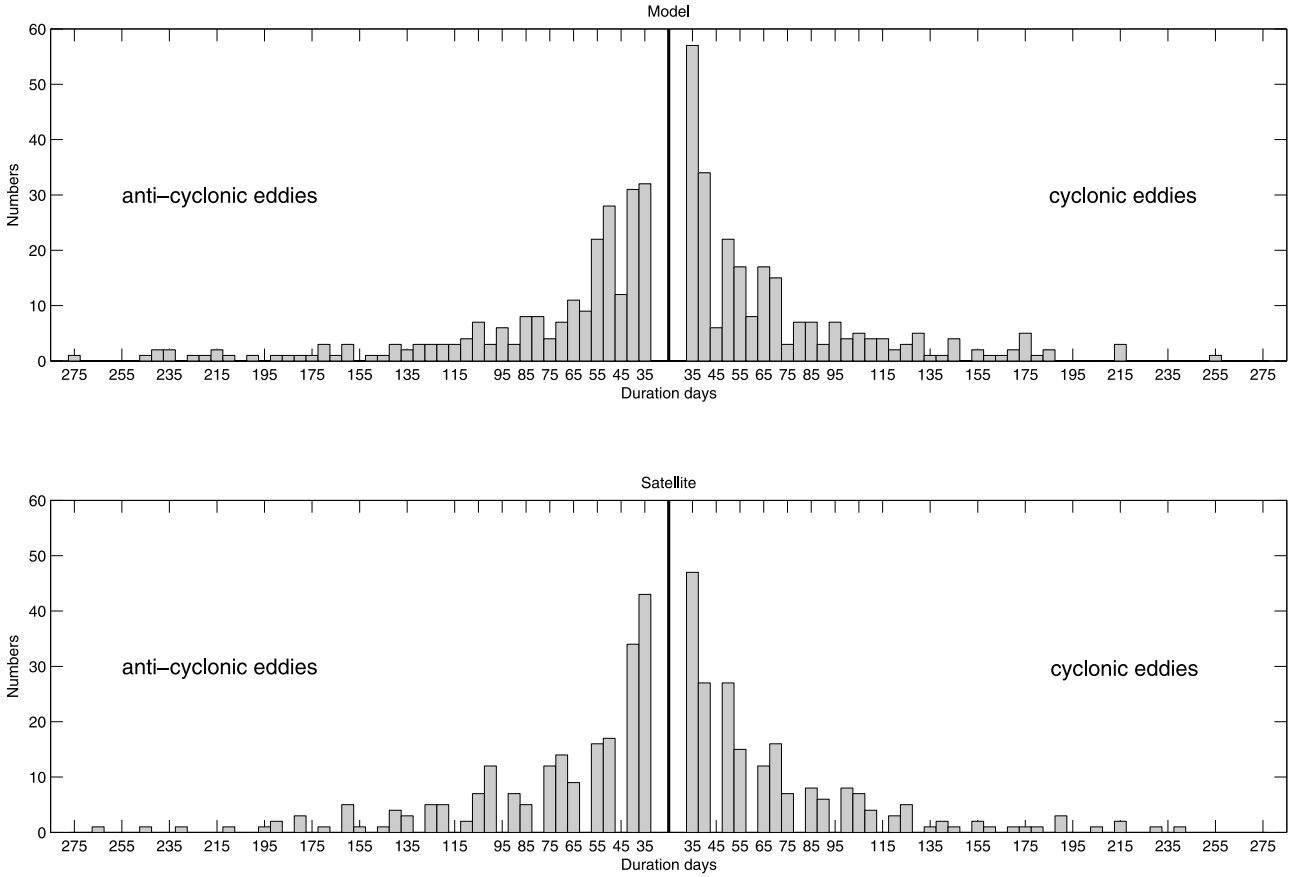

Figure 5. A histogram of the eddy lifetime with an interval of 5 days derived from both the model and the satellite data. Anticyclonic eddies and cyclonic eddies are shown.

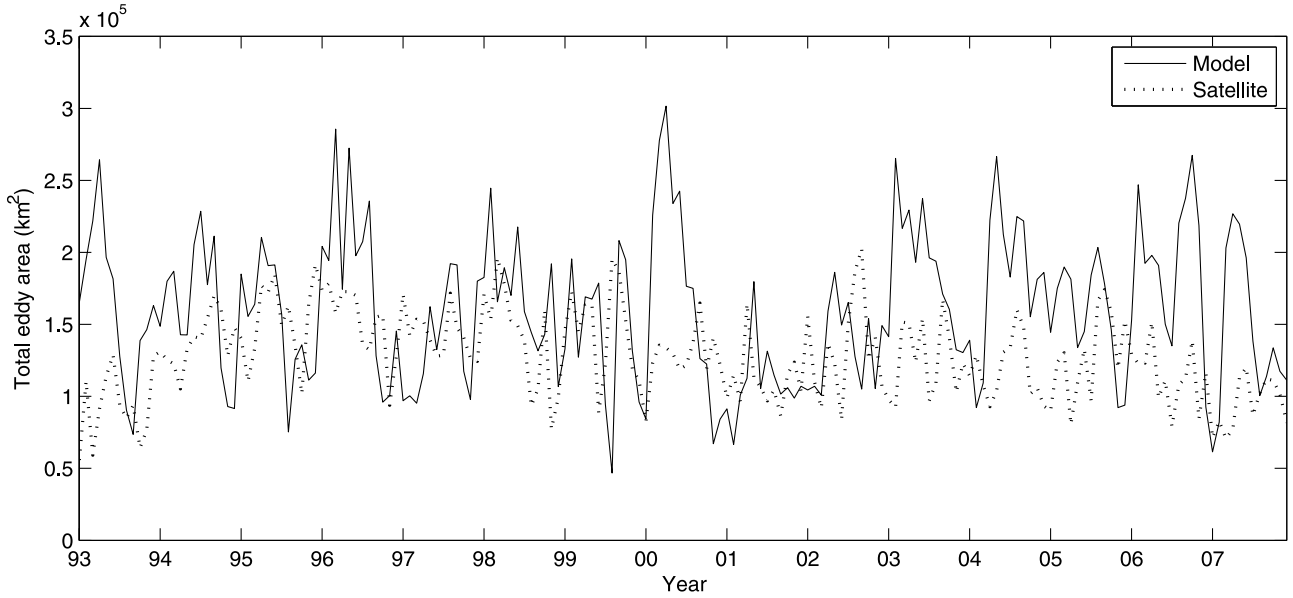

Figure 6. Time series of total eddy area (km^2) in each SLA image averaged by month.

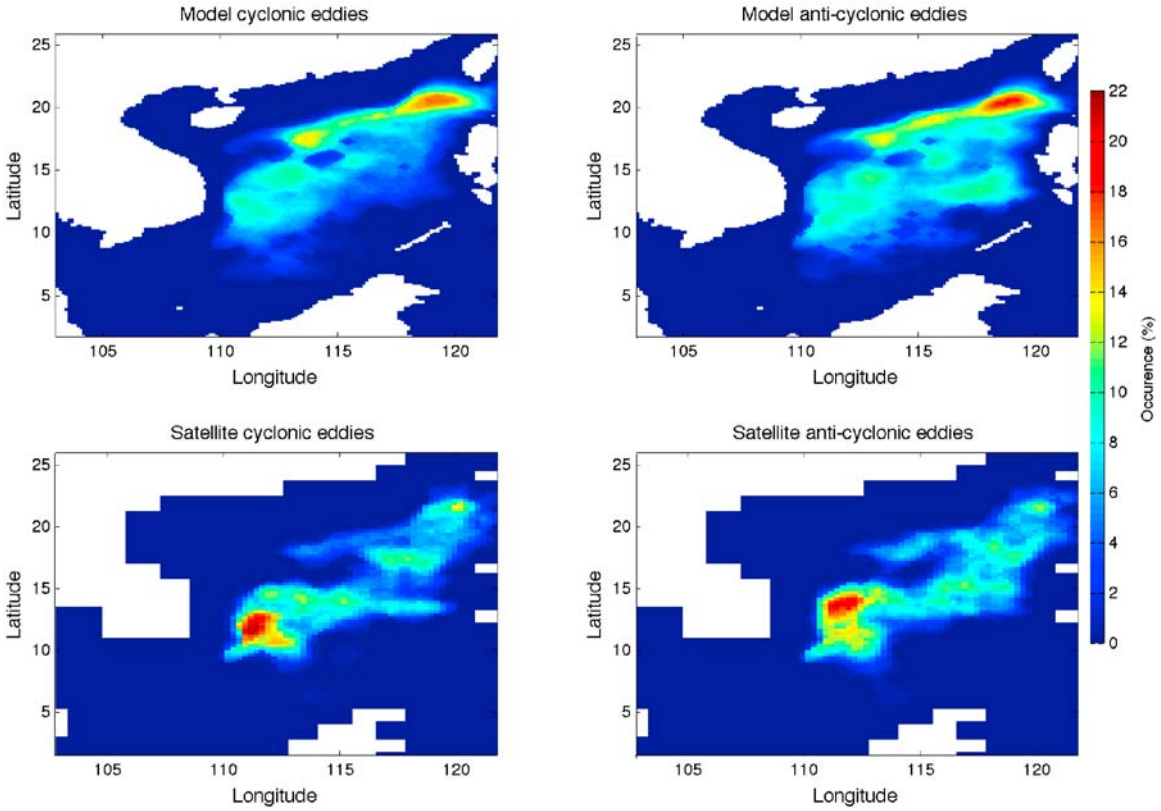

Figure 7. Climatological spatial patterns of eddy occurrence, quantified as the probability at each pixel over the entire time series (1993–2007).

occurs in 1993, 1996, and 2005, and low occurs in 1997, 1998, and 2001. From the satellite, we also see maximum in 1996 and minimum in 1998. The low EKE in 1997 and 1998 is probably the result of a relatively weak wind field under the influence of the 1997–1998 El Niño. Conversely the high EKE during the 1995–1996 is probably caused by the strong wind field under the influence of La Niña. The model captures the basic variability of EKE in terms of the phase, while sometimes overestimates the peaks. The discrepancy between them could result from a number of factors. The difference of horizontal resolution between the satellite data and the model is thought to be an important factor [*Böning and Budich*, 1992; *Oschlies*, 2002]. The finer grid used by the model (1/8° × 1/8°) can resolve smaller structures than the satellite (1/4° × 1/4°), hence it includes more perturbations relative to the mean flow leading to higher EKE values. In addition to the spatial resolution, different time intervals may be another factor affecting EKE estimates, though we already composed monthly data. Original 3 day model output in time step is able to resolve oceanic features that live longer than 6 days, while satellite data with 7 day time step might miss those last for shorter than 2 weeks. Overall, the modeled EKE exhibits similar manner to the satellite data (Table 1). Modeled EKE ranges from 359.7 to 1092.4 $cm^2\ s^{-2}$, with a mean value of 609.7 $cm^2\ s^{-2}$, and satellite derived EKE varies from 409.6 to 767.3 $cm^2\ s^{-2}$, with a mean value of 560.0 $cm^2\ s^{-2}$. The correlation coefficient between these two time series is 0.64 and the relative root mean square error (RMSE) is 9.7%.

[22] We do not observe a consistent correspondence between ENSO events and eddy activities. During the 1995–1996 La Niña year, the SCS circulation was exceptionally energetic, resulting in a very prominent EKE high and hence strong eddy activities in the winter of 1995–1996. On the other hand, EKE in the SCS was relatively weak during the 1998 El Niño year, which agrees well with the EOF result of *Wu et al.* [1998], but strong eddy activities in terms of both numbers and total eddy areas are still observed. Given the premise that ENSO affects the SCS regional wind, which in turn affects the SCS circulation and eddy activities, the discrepancy between ENSO events and eddy activities suggests at the interannual scale wind might not be the only process governing eddy activities and eddy genesis might not be uniform over the entire SCS.

3.2. Eddy Characteristics During 1993–2007

[23] The modeled number of eddies that occur each year agrees well with satellite observations (Figure 4). Our model reproduces the relatively high number around year 1997, but misses the low number in year 2006. On average, there are about 32.9 ± 2.4 eddies predicted by the model and 32.8 ± 3.4 eddies observed by satellite. Of the total eddy numbers, about 52% are cyclonic eddies from both the modeled and satellite data. These results are consistent with the study of *Hwang and Chen* [2000], where they tracked an annual average of 31.1 eddies with 43% of cyclonic eddies during the 1993–1999 period by using T/P altimeter data. However, the recent study of *Wang et al.* [2003] documented an annual average number of about 11 eddies during the 1993–

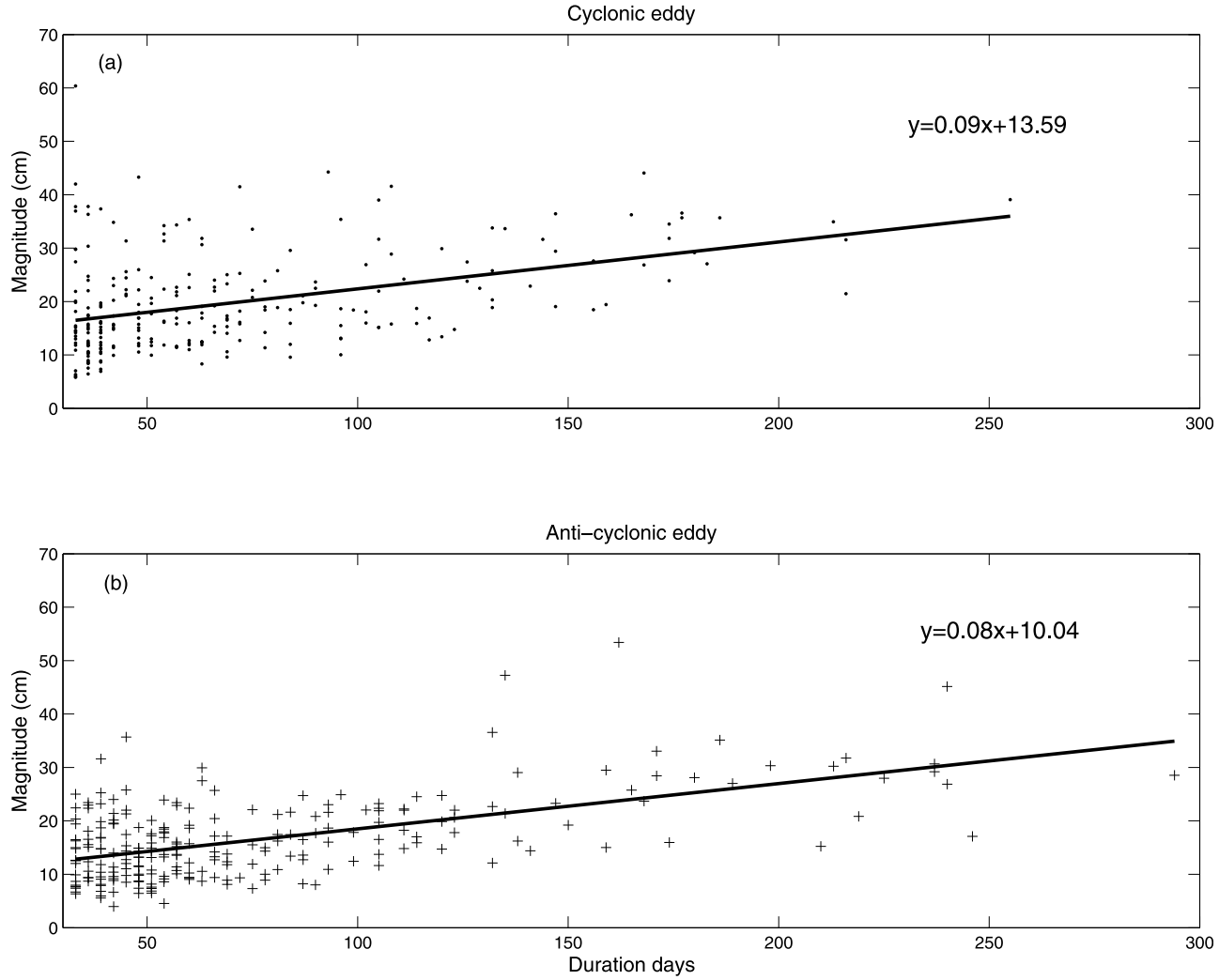

Figure 8. Relationship between eddy lifetime and eddy magnitude (difference between eddy center and eddy edge). The solid lines are the least square fitted lines for cyclonic and anticyclonic eddies.

2000 period by using a multiple altimeter data set. The discrepancy may result from the difference in criteria that were used to identify eddies. *Wang et al.* [2003] focused their studies on those eddies with a typical lifetime about 130 days, and a mean radius around 150 km. While in this work, we also included eddies of smaller sizes (criteria is that the radius larger than 45 km). For the modeled eddies, eddy radius ranges from 46.5 km to 223.5 km, with a mean value of 87.4 km. About 70% of eddies have a radius smaller than 100 km. Smaller eddies tend to be short lived as well. A histogram with an interval of 5 days of the eddy lifetime derived from both the model and satellite data shows that there are many short-lived eddies lasting about 30 days, especially for the cyclonic eddies (31% cyclonic eddies shorter than 40 days for the model; Figure 5). About 53% of the simulated eddies (cyclonic and anticyclonic) have lifetime shorter than 60 days. The histogram is continuous with time only until around 200 days. After that eddy numbers become relatively small and intermittent. Eddy numbers decrease in a general manner with increasing lifetime, though we do observe the exceptions such that the number of eddies with lifetime around 45 days is very small compared with those shorter- or longer-lived eddies.

[24] Another important quantitative measure of eddy activity is the total area in each SLA maps identified as "eddies," not only showing us how many eddies there are but also illustrating how big those areas occupied by eddies are [*Henson and Thomas*, 2008]. The monthly mean of the eddy occupied area is presented in Figure 6. The model captures the interannual variability of the eddy area fairly well in years from 1994 to 2002 except 1996 and 2000, but it overestimates in later years from 2003 to 2007. The mean area covered by eddies is 160,170 km^2 from the model and 127,880 km^2 from satellite, equivalent to about 9.8% and 7.8% of the study area (water depth deeper than 1000 m, equivalent to 4.2% for model and 2.9% for satellite of the entire SCS domain in this study), respectively (Table 1). The eddy-occupied area peaks in 1996, 1999, and 2003, with minima in 1993, 2001, and 2007. This is not quite consistent with EKE time series, because the EKE and eddy area are two different measures of eddy activities. However, we do observe the peaks of EKE in year 1996 and 1999, and minima during 1993 and 2007. *Hwang and Chen* [2000]

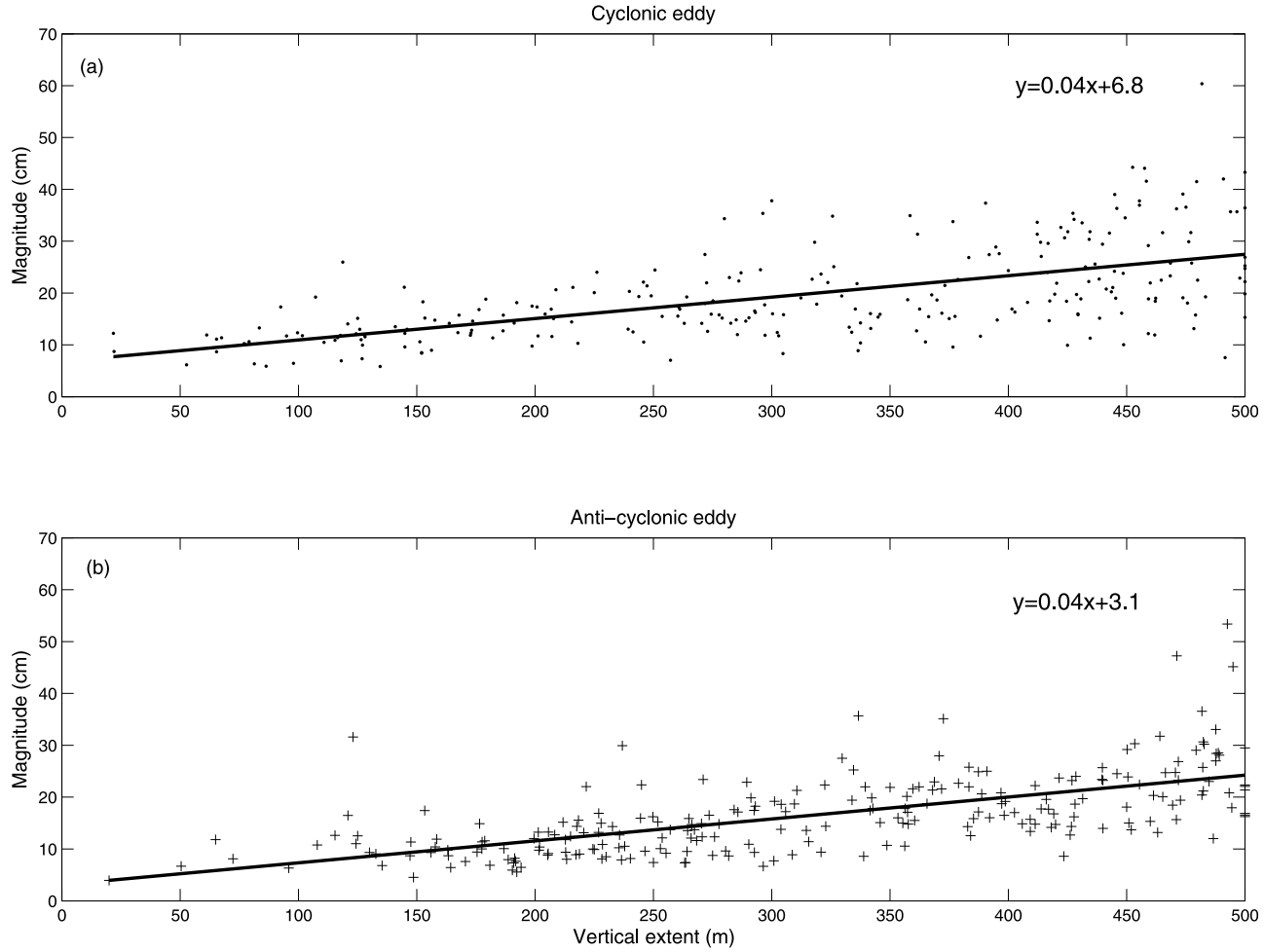

Figure 9. Relationship between eddy vertical extent and eddy magnitude (difference between eddy center and eddy edge). The solid lines are the least square fitted lines for cyclonic and anticyclonic eddies.

also calculated the EKE for the SCS during year 1993–1999. Though with different satellite products, their results show marked similarities to this study.

[25] The spatial distribution of eddies in the SCS is not uniform. Figure 7 shows the climatological spatial distribution of eddies, plotted as the percentage of chance for each pixel when flagged as "eddy." For cyclonic eddies, the model predicts eddies occur most frequently (about 15% of the time) in a patch just west of the Luzon Strait. This agrees well with satellite observation showing the possibility at about 14% in the same area. Model result shows that there is a band stretching from west of the Luzon Strait to the southeast of Hainan Island roughly along the 1000 m bathymetry with a relatively high value around 11%, representing the tracks of westward propagating eddies. This band also shows up in the satellite map although the value is only around 5%, lower than the modeled occurrence. Both the model and satellite data indicate that a high-occurrence patch exists offshore of Vietnam. Our model underestimates the magnitude in this area with the mean value ~9% in the model data compared to ~16% in the satellite data. For anticyclonic eddies, in addition to the band stretching across the northern slope and the offshore patch east of Vietnam, another eddy path is found southwest of the Luzon Island both from the model and the satellite data with probabilities at ~9%. This pattern agrees well with a recent independent study of the intraseasonal variability of sea surface height [*Zhuang et al.*, 2010]. Overall, the model can simulate the general spatial pattern of eddy occurrence. The discrepancy in magnitude between the model and the satellite data especially east of Vietnam is most likely due to the lack of river discharge in the model. Runoff from the Mekong River has profound impacts on water properties and eddy activities even in the southwestern basin [*Ning et al.*, 2004] because of the narrow shelf along the Vietnam coast.

[26] A linear relationship between eddy lifetime and eddy magnitude (sea surface height difference between eddy center and eddy edge) is observed in Figure 8, showing that stronger eddy tends to have longer lifetime, especially for anticyclonic eddies with a better correlation (correlation coefficient is 0.6 for anticyclonic eddies and 0.4 for cyclonic eddies). On the average, cyclonic eddies are stronger than anticyclonic eddies with the mean magnitude of 20 and 17 cm for cyclonic and anticyclonic eddies, respectively. For those eddies with lifetime longer than 200 days, however, about 73% are anticyclonic eddies. The longest duration time is 255 days for cyclonic eddies but 294 days for anticyclonic eddies. In addition to the lifetime, the vertical

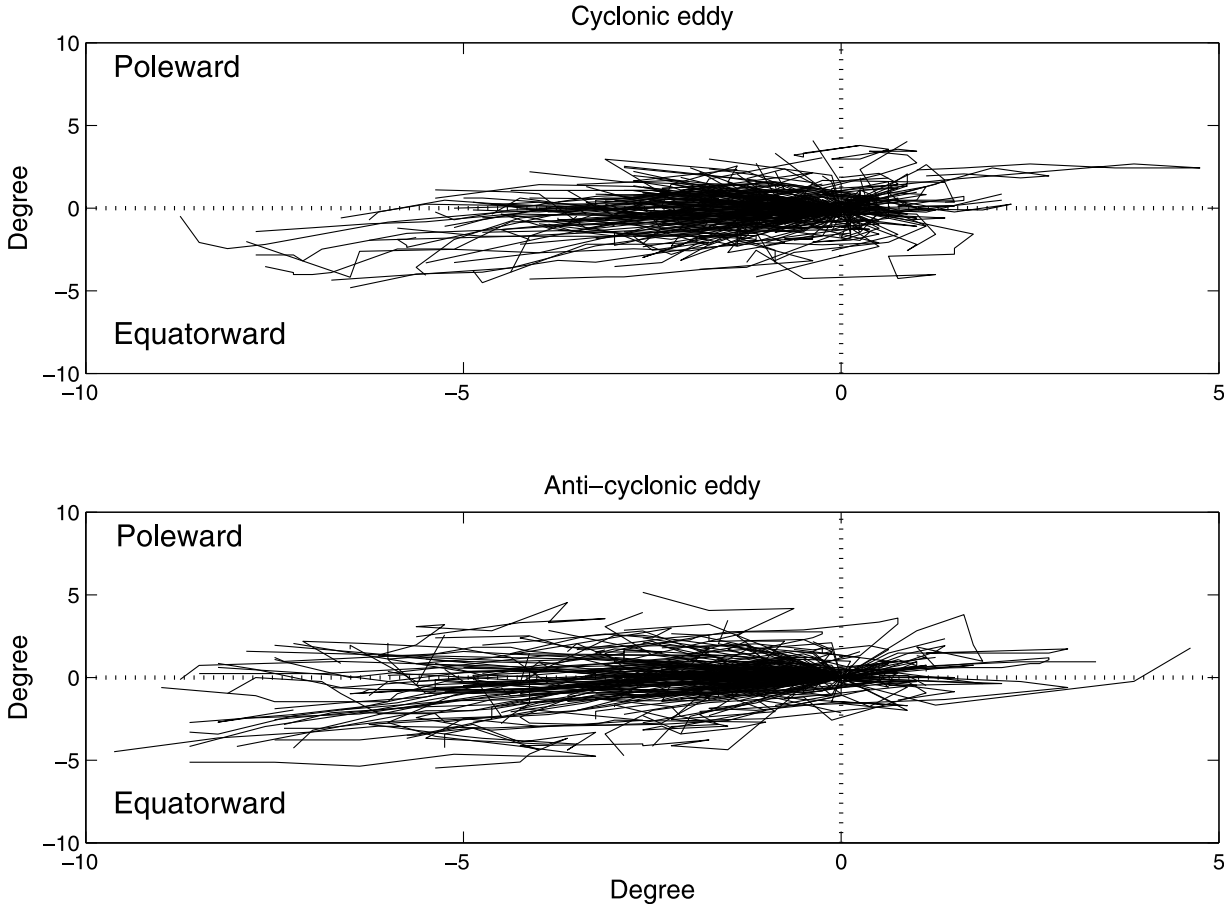

Figure 10. Composite analysis of eddy propagation directions. We put all the eddies together with the same starting point (0,0). The *x* axis denotes the longitude (deg), and *y* axis denotes the latitude (deg).

extent at which an eddy can reach also exhibits a good linear relationship with eddy magnitude (Figure 9), implying stronger eddies tend to influence the ocean deeper than the weaker ones. An interesting point from the least square fit is that fit lines for cyclonic and anticyclonic eddies have the same slope, but that the intercept for cyclonic eddies is a little higher than for anticyclonic eddies, indicating with the same surface eddy magnitude, anticyclonic eddies can influence the ocean interior deeper than cyclonic eddies.

[27] Figure 10 shows the composite analysis of eddy propagation directions. A notable characteristic of the eddy trajectories is the strong tendency for westward propagation such that only about 12% cyclonic eddies and 24% anticyclonic eddies have mean propagation directions that deviate by more than 5° from due west. The proportions of eddies that propagate with equatorward deflection, zonally (±0.5°), and with poleward deflection, respectively, are 49%, 9% and 42% for cyclonic eddies and 41%, 10% and 49% for anticyclonic eddies. The eddy propagation directions predicted by the model are consistent with the theory for nonlinear vortices, which predicts that eddies should propagate westward with small meridional deflections due to the β effect. As eddies rotate they generate an advection of the surrounding fluid in the same direction, which induces small vortices on the flanks of the large vortex. These small vortices finally combine with the large vortex to cause the meridional drift. *Morrow et al.* [2004] confirmed this theory and showed clear pathways of equatorward and poleward deflections for anticyclonic and cyclonic eddies, respectively. On the global basis, *Chelton et al.* [2007] also found that there are slight preferences of poleward deflection for cyclonic eddies and equatorward deflection for anticyclonic eddies. However, our model results do not show these preferences. Conversely, even more cyclonic eddies appear to propagate equatorward. This has not been observed before, and the reason why more cyclonic/anticyclonic eddies propagate equatorward/poleward might be attributed to the combination of β effect and the advection driven by the strong summer and winter monsoons. Eddy meridional drift has a potential effect on the transport of different tracers, such as heat, salt, carbon, nutrients, etc. Statistically, our model results show that the divergence between the warm (anticyclonic) eddies (49% poleward versus 41% equatorward) and cold (cyclonic) eddies (49% equatorward versus 42% poleward) could lead to a net poleward heat transport in the SCS. This agrees with the poleward heat transport of the mean ocean circulation. More quantitative calculations to determine the role of eddies in property and material transport will be conducted in a follow-up study.

3.3. Seasonal Variations of Eddy Characteristics

[28] Previous studies show that eddy lifetimes often show a clear dependence with their place birth [*Chaigneau et al.*, 2008]. While in this study we do not see any spatial pattern

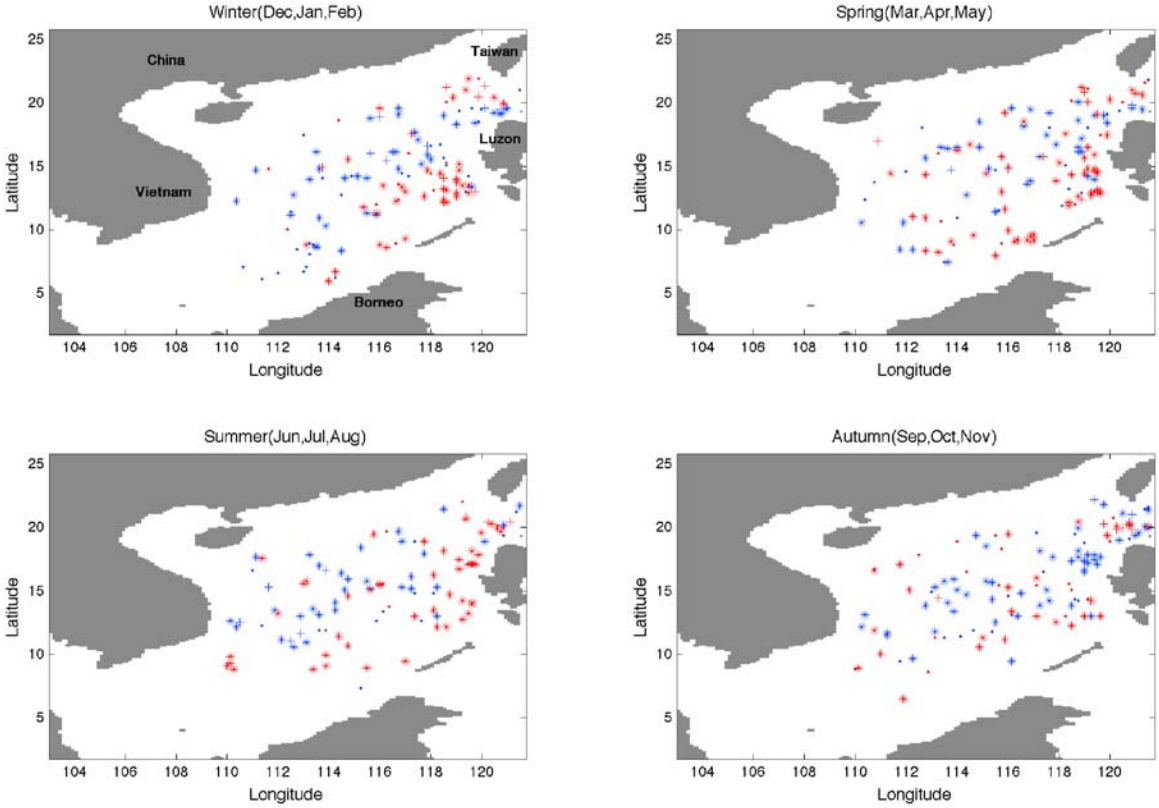

Figure 11. Spatial and seasonal distributions of eddy birthplace. Blue symbols denote cyclonic eddies, and red symbols denote anticyclonic eddies. Circles denote those eddies with a lifetime shorter than 40 days, pluses denote those eddies with a lifetime longer than 150 days, and stars denote the rest.

of the short-lived eddies (Figure 11), but we observe strong seasonal variations of eddy numbers. Autumn and winter seem to be the favorable seasons for generating the short-lived eddies both cyclonic and anticyclonic. This is also true for all of the cyclonic eddies, but it is different for anticyclonic eddies, of which more long-lived ones occur in winter and spring (Figure 12). Another common feature for both cyclonic and anticyclonic eddies is that only a few of them occur in May. This might be caused by variations in the wind, because May is the month when the transition between the northeasterly and the southwesterly monsoon occurs so that the wind stress is the weakest of the year in the SCS [e.g., *Liu and Xie*, 1999].

[29] In winter when the northeasterly monsoon prevails in the SCS with an average wind speed of 9 m s^{-1}, there is generally a cyclonic gyre over the entire deep basin of the SCS. Besides this big gyre, a total of 58 anticyclonic and 73 cyclonic eddies formed in the model for the winter seasons of 1993–2007. Model result indicates two favorable places for the generation of anticyclonic eddies (Figure 11). One is off the southwest of Taiwan close to the Luzon Strait near the Kuroshio intrusion. Frontal instability at the Kuroshio intrusion could be one mechanism in shedding these eddies [*Wang et al.*, 2000; *Su*, 2004]. Another place is off the southwest of Luzon. *Cai et al.* [2002] suggested that the interaction between strong barotropic shelf currents and the local topography is a possible reason for the occurrence of anticyclonic eddies in this area. Long-lived anticyclonic eddies (lifetime longer than 150 days) concentrate mainly off the southwest of Taiwan, and no clear pattern is found for short-lived eddies (lifetime shorter than 40 days). Cyclonic eddies generally form off the northwest of Luzon Island in the deep basin of the SCS. Most of the cyclonic eddies generated in the southern SCS are short lived, while the long-lived cyclonic eddies appear to occur north of 15°N.

[30] An interesting feature in winter is the clustering of two types of eddies near the Luzon Strait (Figure 11). Anticyclonic eddies dominate the northern part, while cyclonic eddies dominate the southern part. This modeled feature agrees well with the previous observations by *G. Wang et al.* [2003, 2008]. Whether Kuroshio intrusion plays a role is still not well understood, but several studies have associated some of the eddies observed in this area with surface wind forcing [*Qu*, 2000; *Metzger*, 2003; *Yang and Liu*, 2003]. These clusters of anticyclonic and cyclonic eddies are found to be correlated with the strong negative and positive wind stress curl, respectively (Figure 13). In winter, northeasterly monsoonal winds are blocked by high mountains on the Luzon and Taiwan Islands, forming a narrow, intense isthmus wind jet through the central Luzon Strait. Associated with the isthmus wind jet, there is a dipole of wind stress curl with negative to the north and positive to the south of the jet. As a result, Ekman pumping on either side of the axis of an offshore wind jet may generate these clusters of anticyclonic and cyclonic eddies [*Willett et al.*, 2006; *G. Wang et al.*, 2008]. Note that our model can reproduce this feature is likely because we use the high-resolution wind

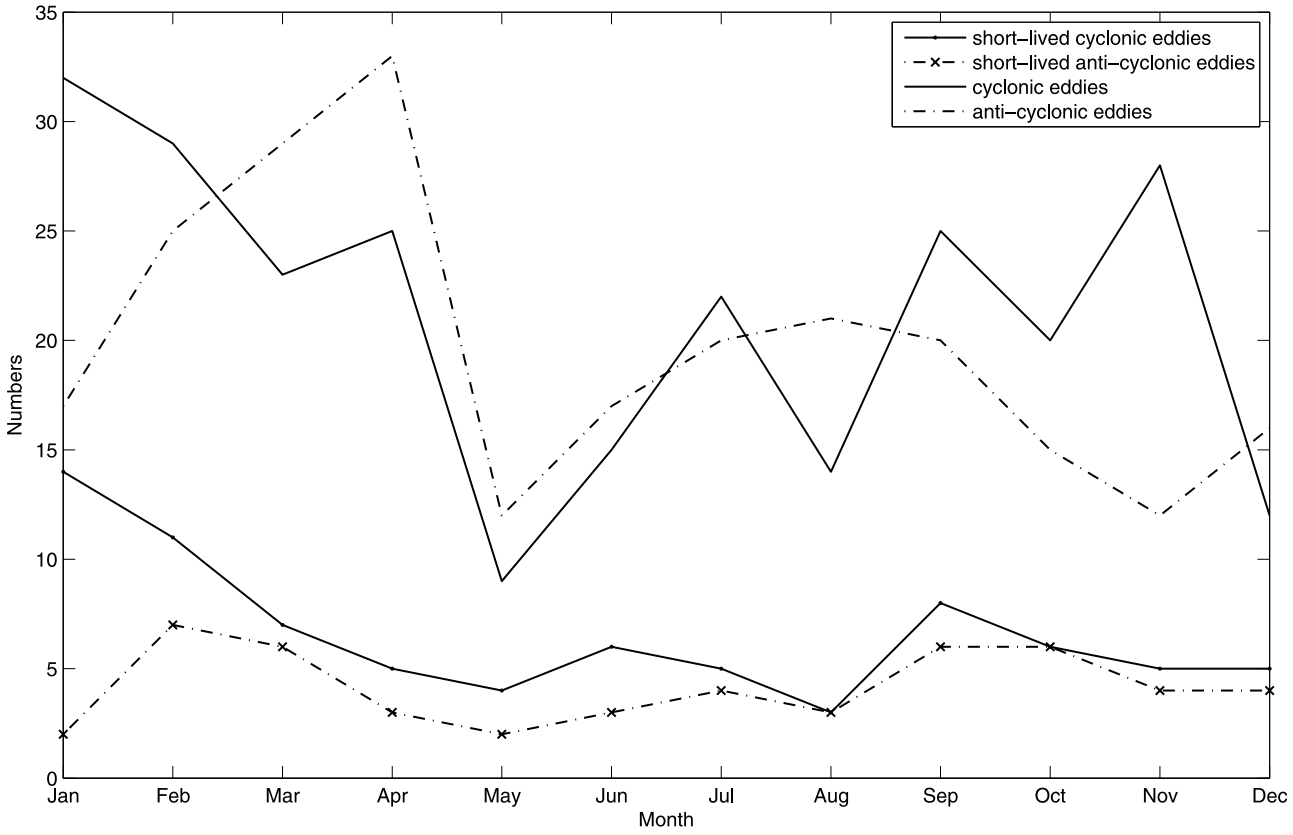

Figure 12. Eddy number distribution, showing the month in which the eddy is initially generated. Here short-lived eddies are those that live for less than 40 days, and long-lived eddies are those that live longer than 150 days.

forcing that resolves wind stress curl fields associated with the gap winds.

[31] In summer, the southwesterly monsoon wind dominates with an average wind speed of 6 m s^{-1}. In all, there are 58 anticyclonic and 51 cyclonic eddies formed for this season in years from 1993 to 2007. Luzon Strait is occupied by more anticyclone eddies and the clustering no longer exists. In addition to the area southwest of Luzon Island, the area northwest of Luzon Island also becomes a breeding ground for anticyclonic eddies. Cyclonic eddies still dominates the central deep basin of the SCS, and only one eddy is found south of 10° N. Several studies show that off the central Vietnam, there is a cyclonic gyre north of about 12° N, but an anticyclonic gyre to the south [*Kuo et al.*, 2000; *Xie et al.*, 2003]. Associated with these gyres is a northward orographic wind jet turning offshore from the Vietnam coast near 12°N. Similar to those eddies near the Luzon Strait in winter, spin-up of cyclonic and anticyclonic eddies on either side of the axis of a wind jet are also reproduced by our model (Figure 13). As a result, off the Vietnam coast, cluster of cyclonic eddies are generated north of 11°N, anticyclonic eddies only occur south of 11°N.

[32] In spring, there are 74 anticyclonic and 57 cyclonic eddies; in autumn, there are 47 anticyclonic and 73 cyclonic eddies predicted by the model, showing us that spring is the most favorable season for anticyclonic eddies and autumn is the most favorable season for cyclonic eddies. Spring and autumn are the two transition seasons between summer and winter monsoons in the SCS, when wind stress decreases to the lowest level of the year. One interesting feature is that more anticyclonic eddies occur in the central basin area in these two seasons than the monsoon season, however, the reason for this is still unclear. In autumn, almost all of the long-lived eddies exist near the Luzon Strait, while in spring, long-lived eddies spread all over the SCS.

4. Summary

[33] A Pacific basin-wide three-dimensional physical model has been developed and the result from a subdomain is used to quantify statistically eddy activities in the SCS for the period from 1993 to 2007. The modeled results are compared with a merged and gridded satellite product of MSLA by using the same eddy identification and tracking method. The modeled eddy activities, on the average, agree well with the satellite data, in terms of the EKE time series, number of eddies, and the total eddy area. There are about 32.8 ± 2.6 eddies predicted by the model and 32.8 ± 3.4 eddies observed by satellite each year, and about 52% of them are cyclonic eddies. The radius of these eddies ranges from about 46.5 km to 223.5 km, with a mean value around 87.4 km. Over 70% eddies have a radius smaller than 100 km. Two linear relationships are observed in this study. The first one is between eddy lifetime and eddy magnitude, and the other one is between eddy vertical extent and eddy magnitude. These two relationships imply that strong eddies usually

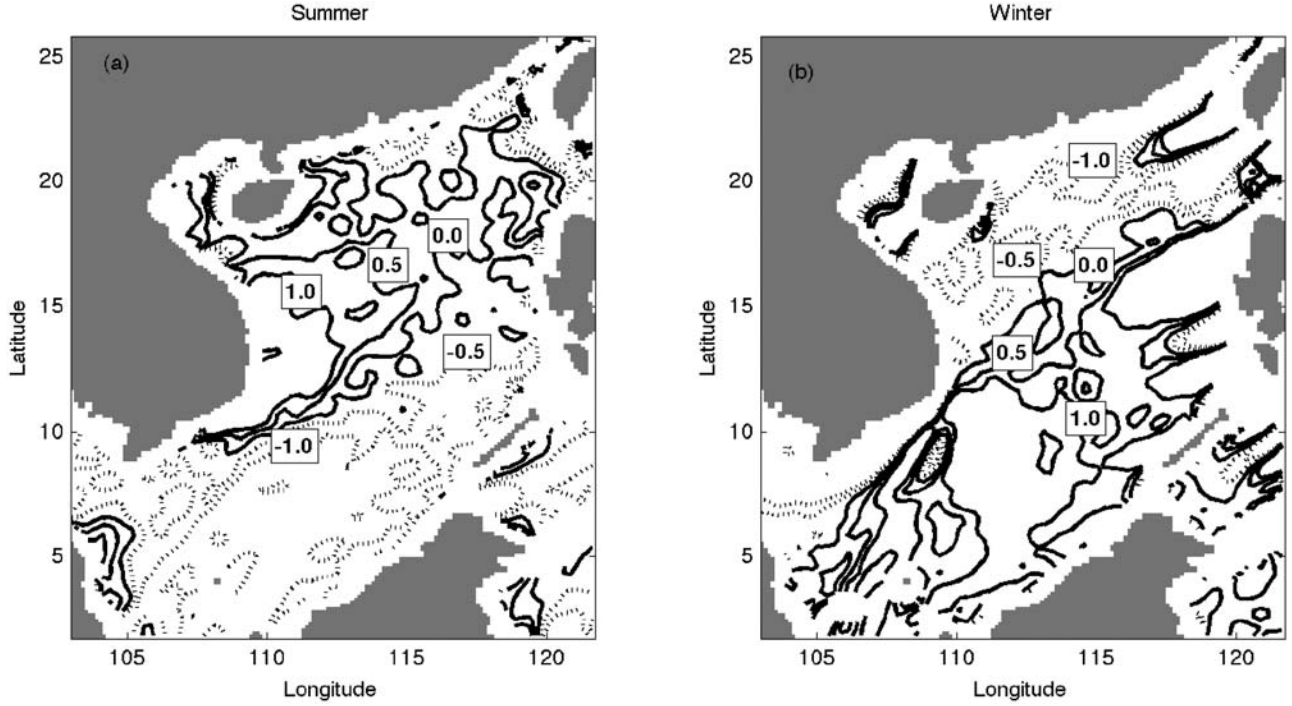

Figure 13. Climatological wind stress curl ($\times 10^{-7}$ N m^{-3}) calculated from 8 years QuikSCAT scatterometer data (1999–2007) [*Risien and Chelton*, 2008]. Solid contours denote positive values, and dashed contours denote negative values. (a) The summer season (June, July, and August), and (b) the winter season (December, January, and February).

can survive much longer and penetrate the ocean much deeper than weak ones. In the SCS, we found about 53% eddies are with a lifetime shorter than 60 days, and about 73% of the long-lived ones are anticyclonic eddies. Model results show that the mean area covered by eddies is 160,170 km^2, equivalent to about 9.8% of the study area (water depth deeper than 1000 m). It is equivalent to about 4.2%, when considering the whole SCS domain. The discrepancy of eddy occurrence between model and satellite implies difficulty in predicting eddy trajectories.

[34] Analysis of eddy propagation directions shows that eddy trajectories have a strong tendency for westward propagation with small meridional deflections. The 49% equatorward deflection compared to 42% poleward deflection for cyclonic eddies versus the 49% poleward deflection compared to 41% equatorward deflection for anticyclonic eddies might lead to a net poleward heat transport in the SCS.

[35] This eddy census quantifies the spatial and temporal variability in the location and properties of both cyclonic and anticyclonic eddies. The SCS circulation is largely driven by the monsoonal winds with seasonally varying directions and is modulated interannually by ENSO. Modeled EKE does not show a good correlation with eddy numbers or occupied area. We suspect there are other important factors in addition to the wind stress affecting eddy formation and tracks.

[36] Previous studies of the SCS by *Wu et al.* [1998] and *Su* [2004] indicate that wind is the major driving force for the upper layer circulation. Conceptually, cyclonic wind stress curl will produce divergence in the surface water and upwelling. Anticyclonic wind stress curl will produce convergence and downwelling. Upwelling brings cold water from the deep to the surface creating cold core eddies, and downwelling deepens the thermocline creating warm core eddies. *Chi et al.* [1998] used this theory to explain the formation of eddies in the central SCS basin. *Hwang and Chen* [2000] compared the wind stress curl and eddies in the central SCS basin. They found that positive (negative) wind stress curl anomaly corresponded to a cold core (warm core) eddy whose angular velocity is positive (negative), while the coherence between wind stress curl anomaly and EKE is not significant at the interannual scales as the wind variability in the SCS is predominantly seasonal. In addition to the wind stress curl, indirect influences of wind may also play a role in the formation of eddies. The cyclonic eddies east of Vietnam in summer are generated in a different way from that in the central SCS basin. In summer, the southwesterly monsoonal wind stress parallel to the coast of Vietnam drives the water to the right of the wind because of the Ekman effect, resulting in upwelling of cold water, which in turn leads to the generation of cold core eddies [*Hwang and Chen*, 2000]. As discussed above, the orographic wind jets associated with the northeasterly winter monsoon and the gaps between the islands can also spin up cyclonic and anticyclonic eddies west of the Luzon Strait. While eddies southwest of the Luzon Island are thought to be generated by the interaction between strong barotropic shelf currents and the local topography. Since the SCS is part of the Pacific system, connections between the SCS and Pacific Ocean through Luzon Strait are also thought to be important for the eddy genesis. *Hu et al.* [2001] suggested

that 3–6 month sea surface height fluctuation in the West Pacific Subtropical Counter Current region might propagate into the SCS and generate mesoscale eddies. Although Kuroshio appears as a barrier to the westward propagating eddies from the Pacific Ocean, *Li et al.* [2007] observed that the 45 day SLA fluctuation, which is thought to be the mesoscale variability from the Kuroshio is able to propagate into the SCS via the Luzon Strait. Other mechanisms such as the instabilities of the background currents and the instability of Rossby waves are also likely to generate eddies in the SCS. All these may explain why we do not see robust correlation between the EKE and total eddy areas in this study.

[37] Eddies are thought to be important to cross-shelf exchanges of heat, salt, momentum, and biogeochemical properties, which further affect ocean biology. Cyclonic eddies uplift the isopycnals due to upwelling, which in turn enrich the oligotrophic surface layers. In the presence of adequate sunlight, this leads to enhanced rates of biological productivity. In the case of anticyclonic eddies, the nutrient poor surface water are pushed down to deep layers and usually do not result in obvious ecosystem response, though sometimes nutrient depletion near the surface caused by anticyclonic eddies could result in phytoplankton species succession [*Ning et al.*, 2004]. In the SCS, eddies moving with enhanced chlorophyll have been observed by satellite in many studies [*Tang et al.*, 2002; *Chen et al.*, 2007; *Chow et al.*, 2008]. As a result, the westward propagating eddies might contribute to the high primary productivity and carbon export in the coastal regions in the western SCS [*Ning et al.*, 2004]. Recently, the physical model used in this study has been successfully coupled with a biogeochemical model, CoSiNE model [*Chai et al.*, 2002; *Dugdale et al.*, 2002]. Based on these identified eddies, the results from the coupled model will allow us further to investigate the role of eddies in biological response, primary and export productions, as well as carbon and nitrogen cycling.

[38] **Acknowledgments.** This research was supported by a NASA grant (NNG04GM64G) and NSFC grant (90711006) to F. Chai. This research was carried out, in part, by the Jet Propulsion Laboratory (JPL), California Institute of Technology, under contract with the National Aeronautics and Space Administration (NASA).

References

Basdevant, C., and T. Philipovitch (1994), On the validity of the "Weiss criterion" in two-dimensional turbulence, *Physica D*, *73*, 17–30, doi:10.1016/0167-2789(94)90222-4.

Böning, C. W., and R. G. Budich (1992), Eddy dynamics in a primitive equation model: Sensitivity to horizontal resolution and friction, *J. Phys. Oceanogr.*, *22*, 361–381, doi:10.1175/1520-0485(1992)022<0361:EDIAPE>2.0.CO;2.

Cai, S. Q., J. L. Su, Z. J. Gan, and Q. Y. Liu (2002), The numerical study of the South China Sea upper circulation characteristics and its dynamic mechanism in winter, *Cont. Shelf Res.*, *22*, 2247–2264, doi:10.1016/S0278-4343(02)00073-0.

Calil, P. H. R., K. J. Richards, Y. Jia, and R. R. Bidigare (2008), Eddy activity in the lee of the Hawaiian Islands, *Deep Sea Res. Part II*, *55*, 1179–1194, doi:10.1016/j.dsr2.2008.01.008.

Chai, F., R. C. Dugdale, T. H. Peng, F. P. Wilkerson, and R. T. Barber (2002), One dimensional ecosystem model of the equatorial Pacific upwelling system. Part 1. Model development and silicon and nitrogen cycle, *Deep Sea Res. Part II*, *49*, 2713–2745, doi:10.1016/S0967-0645(02)00055-3.

Chaigneau, A., A. Gizolme, and C. Grados (2008), Mesoscale eddies off Peru in altimeter records: Identification algorithms and eddy spatio-temporal patterns, *Prog. Oceanogr.*, *79*, 106–119, doi:10.1016/j.pocean.2008.10.013.

Chelton, D. B., M. G. Schlax, R. M. Samelson, and R. A. de Szoeke (2007), Global observations of large oceanic eddies, *Geophys. Res. Lett.*, *34*, L15606, doi:10.1029/2007GL030812.

Chen, Y. L., H. Y. Chen, I. I. Lin, M. A. Lee, and J. Chang (2007), Effects of cold eddy on phytoplankton production and assemblages in Luzon Strait bordering the South China Sea, *J. Oceanogr.*, *63*, 671–683, doi:10.1007/s10872-007-0059-9.

Chi, P. C., Y. Chen, and S. Lu (1998), Wind-driven South China Sea deep basin warm-core/cool core eddies, *J. Oceanogr.*, *54*, 347–360, doi:10.1007/BF02742619.

Chow, C., J. Hu, L. R. Centurioni, and P. P. Niiler (2008), Mesoscale Dongsha Cyclonic Eddy in the northern South China Sea by drifter and satellite observations, *J. Geophys. Res.*, *113*, C04018, doi:10.1029/2007JC004542.

Doglioli, A. M., B. Blanke, S. Speich, and G. Lapeyre (2007), Tracking coherent structures in a regional ocean model with wavelet analysis: Application to Cape Basin eddies, *J. Geophys. Res.*, *112*, C05043, doi:10.1029/2006JC003952.

d'Ovidio, F., J. Isern-Fontanet, C. López, E. Hernández-García, and E. García-Ladona (2009), Comparison between Eulerian diagnostics and finite-size Lyapunov exponents computed from altimetry in the Algerian basin, *Deep Sea Res. Part I*, *56*, 15–31, doi:10.1016/j.dsr.2008.07.014.

Ducet, N., P. Y. Le Traon, and G. Reverdin (2000), Global high resolution mapping of ocean circulation from TOPEX/Poseidon and ERS-1 and -2, *J. Geophys. Res.*, *105*, 19,477–19,478, doi:10.1029/2000JC900063.

Dugdale, R. C., R. T. Barber, F. Chai, T. H. Peng, and F. P. Wilkerson (2002), One dimensional ecosystem model of the equatorial Pacific upwelling system. Part 2. Sensitivity analysis and comparison with JGOFS EqPac data, *Deep Sea Res. Part II*, *49*, 2746–2762.

Fang, G., H. Chen, Z. Wei, Y. Wang, X. Wang, and C. Li (2006), Trends and interannual variability of the South China Sea surface winds, surface height, and surface temperature in the recent decade, *J. Geophys. Res.*, *111*, C11S16, doi:10.1029/2005JC003276.

Fang, W. D., G. H. Fang, P. Shi, Q. Z. Huang, and Q. Xie (2002), Seasonal structures of upper layer circulation in the southern South China Sea from in situ observations, *J. Geophys. Res.*, *107*(C11), 3202, doi:10.1029/2002JC001343.

Gan, J., H. Li, E. N. Curchitser, and D. B. Haidvogel (2006), Modeling South China Sea circulation: Response to seasonal forcing regimes, *J. Geophys. Res.*, *111*, C06034, doi:10.1029/2005JC003298.

He, Z., D. Wang, and J. Hu (2002), Features of eddy kinetic energy and variations of upper circulation in the South China Sea, *Acta Oceanol. Sin.*, *21*, 305–314.

Henson, S., and A. C. Thomas (2008), A census of oceanic anticyclonic eddies in the Gulf of Alaska, *Deep Sea Res. Part I*, *55*, 163–176, doi:10.1016/j.dsr.2007.11.005.

Hu, J., H. Kawamura, H. Hong, and Y. Qi (2000), A review on the currents in the South China Sea: Seasonal circulation, South China Sea warm current and Kuroshio intrusion, *J. Oceanogr.*, *56*, 607–624, doi:10.1023/A:1011117531252.

Hu, J., H. Kawamura, H. Hong, F. Kobashi, and D. Wang (2001), 3≈6 month variation of sea surface height in the South China Sea and its adjacent ocean, *J. Oceanogr.*, *57*, 69–78, doi:10.1023/A:1011126804461.

Hwang, C., and S. Chen (2000), Circulations and eddies over the South China Sea derived from TOPEX/Poseidon altimetry, *J. Geophys. Res.*, *105*, 23,943–23,965, doi:10.1029/2000JC900092.

Isern-Fontanet, J., E. Garcia-Ladona, and J. Font (2003), Identification of marine eddies from altimetric maps, *J. Atmos. Oceanic Technol.*, *20*, 772–778, doi:10.1175/1520-0426(2003)20<772:IOMEFA>2.0.CO;2.

Isern-Fontanet, J., E. Garcia-Ladona, and J. Font (2006), Vortices of the Mediterranean Sea: An altimetric perspective, *J. Phys. Oceanogr.*, *36*, 87–103, doi:10.1175/JPO2826.1.

Jia, Y., and Q. Liu (2004), Eddy shedding from the Kuroshio Bend at Luzon Strait, *J. Oceanogr.*, *60*, 1063–1069, doi:10.1007/s10872-005-0014-6.

Jia, Y., Q. Liu, and W. Liu (2005), Primary study of the mechanism of eddy shedding from the Kuroshio Bend in Luzon Strait, *J. Oceanogr.*, *61*, 1017–1027, doi:10.1007/s10872-006-0018-x.

Kalnay, E., et al. (1996), The NCEP/NCAR 40-year reanalysis project, *Bull. Am. Meteorol. Soc.*, *77*, 437–471, doi:10.1175/1520-0477(1996)077<0437:TNYRP>2.0.CO;2.

Kuo, N. J., Q. Zheng, and C. R. Ho (2000), Satellite observation of upwelling along the western coast of the South China Sea, *Remote Sens. Environ.*, *74*, 463–470, doi:10.1016/S0034-4257(00)00138-3.

Kuo, N. J., Q. A. Zheng, and C. R. Ho (2004), Response of Vietnam coastal upwelling to the 1997–1998 ENSO event observed by multisensor data, *Remote Sens. Environ.*, *89*, 106–115, doi:10.1016/j.rse.2003.10.009.

Large, W. G., and S. Pond (1982), Sensible and latent heat flux measurements over the ocean, *J. Phys. Oceanogr.*, *12*, 464–482, doi:10.1175/1520-0485(1982)012<0464:SALHFM>2.0.CO;2.

Li, L., W. D. Nowlin, and J. Su (1998), Anticyclonic rings from the Kuroshio in the South China Sea, *Deep Sea Res. Part I*, *45*, 1469–1482, doi:10.1016/S0967-0637(98)00026-0.

Li, L., C. Jing, and D. Zhu (2007), Coupling and propagating of mesoscale sea level variability between the western Pacific and the South China Sea, *Chin. Sci. Bull.*, *52*, 1699–1707, doi:10.1007/s11434-007-0203-3.

Liu, Q., X. Jiang, S.-P. Xie, and W. T. Liu (2004), A gap in the Indo-Pacific warm pool over the South China Sea in boreal winter: Seasonal development and interannual variability, *J. Geophys. Res.*, *109*, C07012, doi:10.1029/2003JC002179.

Liu, Q., A. Kaneko, and J. Su (2008), Recent progress in studies of the South China Sea circulation, *J. Oceanogr.*, *64*, 753–762, doi:10.1007/s10872-008-0063-8.

Liu, W. T., and X. Xie (1999), Space-based observations of the seasonal changes of South Asian monsoons and oceanic response, *Geophys. Res. Lett.*, *26*, 1473–1476, doi:10.1029/1999GL900289.

Metzger, E. J. (2003), Upper ocean sensitivity to wind forcing in the South China Sea, *J. Oceanogr.*, *59*, 783–798, doi:10.1023/B:JOCE.0000009570.41358.c5.

Morrow, R., F. Birol, D. Griffin, and J. Sudre (2004), Divergent pathways of cyclonic and anticyclonic ocean eddies, *Geophys. Res. Lett.*, *31*, L24311, doi:10.1029/2004GL020974.

Ning, X., F. Chai, H. Xue, Y. Cai, C. Liu, G. Zhu, and J. Shi (2004), Physical-biological oceanographic coupling influencing phytoplankton and primary production in the South China Sea, *J. Geophys. Res.*, *109*, C10005, doi:10.1029/2004JC002365.

Okubo, A. (1970), Horizontal dispersion of floatable particles in the vicinity of velocity singularity such as convergences, *Deep Sea Res.*, *17*, 445–454.

Oschlies, A. (2002), Improved representation of upper-ocean dynamics and mixed layer depths in a model of the North Atlantic on switching from eddy-permitting to eddy-resolving grid resolution, *J. Phys. Oceanogr.*, *32*, 2277–2298, doi:10.1175/1520-0485(2002)032<2277:IROUOD>2.0.CO;2.

Qiu, B., and S. Chen (2005), Eddy-induced heat transport in the subtropical North Pacific from Argo, TMI and altimetry measurements, *J. Phys. Oceanogr.*, *35*, 458–473, doi:10.1175/JPO2696.1.

Qu, T. (2000), Upper-layer circulation in the South China Sea, *J. Phys. Oceanogr.*, *30*, 1450–1460, doi:10.1175/1520-0485(2000)030<1450:ULCITS>2.0.CO;2.

Qu, T., Y. Y. Kim, M. Yaremchuk, T. Tozuka, A. Ishida, and T. Yamagata (2004), Can Luzon Strait transport play a role in conveying the impact of ENSO to the South China Sea?, *J. Clim.*, *17*, 3644–3657, doi:10.1175/1520-0442(2004)017<3644:CLSTPA>2.0.CO;2.

Qu, T., Y. Du, G. Meyers, A. Ishida, and D. Wang (2005), Connecting the tropical Pacific with Indian Ocean through South China Sea, *Geophys. Res. Lett.*, *32*, L24609, doi:10.1029/2005GL024698.

Qu, T., Y. T. Song, and T. Yamagata (2009), An introduction to the South China Sea throughflow: Its dynamics, variability, and application for climate, *Dyn. Atmos. Oceans*, *47*, 3–14, doi:10.1016/j.dynatmoce.2008.05.001.

Risien, C. M., and D. B. Chelton (2008), A global climatology of wind and wind stress fields from eight years of QuikSCAT scatterometer data, *J. Phys. Oceanogr.*, *38*, 2379–2413, doi:10.1175/2008JPO3881.1.

Shaw, P. T., S. Y. Chao, and L. Fu (1999), Sea surface height variations in the South China Sea from satellite altimetery, *Oceanol. Acta*, *22*, 1–17, doi:10.1016/S0399-1784(99)80028-0.

Soong, Y. S., J. H. Hu, C. R. Ho, and P. P. Niiler (1995), Cold-core eddy detected in South China Sea, *Eos Trans. AGU*, *76*, 345, doi:10.1029/95EO00209.

Su, J. (2004), Overview of the South China Sea circulation and its influence on the coastal physical oceanography outside the Pearl River Estuary, *Cont. Shelf Res.*, *24*, 1745–1760, doi:10.1016/j.csr.2004.06.005.

Tang, D., H. Kawamura, and A. J. Luis (2002), Short-term variability of phytoplankton blooms associated with a clod eddy on the north-western Arabian Sea, *Remote Sens. Environ.*, *81*, 82–89, doi:10.1016/S0034-4257(01)00334-0.

Wang, D., Q. Liu, R. Huang, Y. Du, and T. Qu (2006), Interannual variability of the South China Sea throughflow inferred from wind data and an ocean data assimilation product, *Geophys. Res. Lett.*, *33*, L14605, doi:10.1029/2006GL026316.

Wang, D., H. Xu, J. Lin, and J. Hu (2008), Anticyclonic eddies in the northeastern South China Sea during winter 2003/2004, *J. Oceanogr.*, *64*, 925–935, doi:10.1007/s10872-008-0076-3.

Wang, G., J. Su, and P. C. Chu (2003), Mesoscale eddies in the South China Sea detected from altimeter data, *Geophys. Res. Lett.*, *30*(21), 2121, doi:10.1029/2003GL018532.

Wang, G., D. Chen, and J. Su (2008), Winter Eddy Genesis in the Eastern South China Sea due to Orographic Wind Jets, *J. Phys. Oceanogr.*, *38*, 726–732, doi:10.1175/2007JPO3868.1.

Wang, L., C. J. Koblinsky, and S. Howden (2000), Mesoscale variability in the south china sea from the TOPEX/Poseidon altimetry data, *Deep Sea Res. Part I*, *47*, 681–708, doi:10.1016/S0967-0637(99)00068-0.

Wang, X., and Y. Chao (2004), Simulated sea surface salinity variability in the tropical Pacific, *Geophys. Res. Lett.*, *31*, L02302, doi:10.1029/2003GL018146.

Waugh, D. W., E. R. Abraham, and M. M. Bowen (2006), Spatial variations of stirring in the surface ocean: A case study of the Tasman Sea, *J. Phys. Oceanogr.*, *36*, 526–542, doi:10.1175/JPO2865.1.

Weiss, J. (1991), The dynamics of enstrophy transfer in two dimensional hydrodynamics, *Physica D*, *48*, 273–294, doi:10.1016/0167-2789(91)90088-Q.

Willett, C. S., R. R. Leben, and M. F. L. Peregrina (2006), Eddies and tropical instability waves in the eastern tropical Pacific: A review, *Prog. Oceanogr.*, *69*, 218–238, doi:10.1016/j.pocean.2006.03.010.

Wu, C. R., and T. L. Chiang (2007), Mesoscale eddies in the northern South China Sea, *Deep Sea Res. Part II*, *54*, 1575–1588, doi:10.1016/j.dsr2.2007.05.008.

Wu, C. R., P. T. Shaw, and S. Y. Chao (1998), Seasonal and interannual variations in the velocity field of the South China Sea, *J. Oceanogr.*, *54*, 361–372, doi:10.1007/BF02742620.

Wunsch, C. (1999), Where do ocean eddy heat fluxes matter?, *J. Geophys. Res.*, *104*, 13,235–13,250, doi:10.1029/1999JC900062.

Wyrtki, K. (1961), Physical oceanography of the Southeast Asian waters: Scientific results of marine investigations of the South China Sea and the Gulf of Thailand, *Naga Rep. 2*, 195 pp., Scripps Inst. of Oceanogr., La Jolla, Calif.

Xie, S. P., Q. Xie, D. Wang, and W. T. Liu (2003), Summer upwelling in the South China Sea and its role in regional climate variations, *J. Geophys. Res.*, *108*(C8), 3261, doi:10.1029/2003JC001867.

Xue, H., F. Chai, N. Pettigrew, D. Xu, M. Shi, and J. Xu (2004), Kuroshio intrusion and the circulation in the South China Sea, *J. Geophys. Res.*, *109*, C02017, doi:10.1029/2002JC001724.

Yang, H., and Q. Y. Liu (2003), Forced Rossby wave in the northern South China Sea, *Deep Sea Res.*, *50*, 917–926, doi:10.1016/S0967-0637(03)00074-8.

Yaremchuk, M., and T. Qu (2004), Seasonal variability of the circulation near the Philippine coast, *J. Phys. Oceanogr.*, *34*, 844–855, doi:10.1175/1520-0485(2004)034<0844:SVOTLC>2.0.CO;2.

Yuan, D., W. Han, and D. Hu (2007), Anticyclonic eddies northwest of Luzon in summer–fall observed by satellite altimeters, *Geophys. Res. Lett.*, *34*, L13610, doi:10.1029/2007GL029401.

Zhang, H. M., J. J. Bates, and R. W. Reynolds (2006), Assessment of composite global sampling: Sea surface wind speed, *Geophys. Res. Lett.*, *33*, L17714, doi:10.1029/2006GL027086.

Zhuang, W., S.-P. Xie, D. Wang, B. Taguchi, H. Aiki, and H. Sasaki (2010), Intraseasonal variability in sea surface height over the South China Sea, *J. Geophys. Res.*, doi:10.1029/2009JC005647, in press.

F. Chai, L. Shi, H. Xue, and P. Xiu, School of Marine Sciences, University of Maine, Orono, ME 04469, USA. (fchai@maine.edu)

Y. Chao, Jet Propulsion Laboratory, California Institute of Technology, 4800 Oak Grove Dr., Pasadena, CA 91109-8001, USA.